Article:

Wittkop, C, Swanner, ED, Grengs, A et al. (2020) Evaluating a primary carbonate pathway for manganese enrichments in reducing environments. Earth and Planetary Science Letters, 538. 116201. ISSN: 0012-821X

https://doi.org/10.1016/j.epsl.2020.116201

Manuscript for Earth and Planetary Science Letters

Title: Evaluating a primary carbonate pathway for manganese enrichments in reducing environments

Authors: Chad Wittkop*(1), Elizabeth D. Swanner (2), Ashley Grengs (1), Nicholas Lambrecht (2), Mojtaba Fakhraee (3), Amy Myrbo (4), Andrew W. Bray (5), Simon W. Poulton (5), and Sergei Katsev (3,6)

*Corresponding author, chad.wittkop@mnsu.edu, 507-389-6929

(1)Department of Chemistry and Geology, Minnesota State University, 241 Ford Hall, Mankato, MN 56001

(2)Department of Geological and Atmospheric Sciences, Iowa State University, 2337 Osborn Drive, Ames, IA, 50011

(3)Large Lakes Observatory, University of Minnesota Duluth 2205 East 5th Street, Duluth, MN 55812

(4) St. Croix Watershed Research Station, Science Museum of Minnesota, 16910 152nd St North, Marine on St. Croix, MN 55047 (5) School of Earth and Environment, University of Leeds, Leeds LS2 9JT, UK

(6)Department of Physics, University of Minnesota Duluth, 1049 University Drive, Duluth, MN 55812

Abstract

Most manganese (Mn) enrichments in the sedimentary rock record are hosted in carbonate minerals, which are assumed to have formed by diagenetic reduction of precursor Mn-oxides, and are considered diagnostic of strongly oxidizing conditions. Here we explore an alternative model where Mn-carbonates form in redox-stratified water columns linked to calcium carbonate dissolution. In ferruginous Brownie Lake in Minnesota, USA, we document Mn-carbonates as an HCl-extractable phase present in sediment traps and in reducing portions of the water column. Mn-carbonate become supersaturated in the Brownie Lake chemocline where dissolved oxygen concentrations fall below 5 μM, and Mn-oxide reduction increases the dissolved Mn concentration. Supersaturation is enhanced when calcite originating from surface waters dissolves in more acidic waters at the chemocline. In the same zone, sulfate reduction and microaerobic methane oxidation add dissolved inorganic carbon (DIC) with negative $\delta^{13}C$. These observations demonstrate that sedimentary Mn enrichments may 1) develop from primary carbonate phases, and 2) can occur in environments with dissolved oxygen concentrations <5 μM. Primary Mn-carbonates are likely to originate in environments with high concentrations of dissolved Mn (>200 μM), and where Mn and Fe are partitioned by S cycling, photoferrotrophy, or microaerophilic Fe-oxidation. A shallow lysocline enhances Mn-carbonate production by providing additional DIC and nucleation sites for crystal growth. This carbonate model for Mn-enrichments is expected to be viable in both euxinic and ferruginous environments, and provides a more nuanced view

of the relationships between Mn and carbon cycling, with applications throughout the rock record.

Word count

6483/6500 (1/14/20)

1. Introduction

The strong oxidizing potential (E = 1.228 V) required to form insoluble Mn(IV) oxides (e.g. MnO_2, pyrolusite) from reduced and dissolved Mn(II) make sedimentary Mn enrichments (SMEs) a proxy for the accumulation of oxygen in Earth's early atmosphere and oceans (Kirschvink et al., 2000; Planavsky et al., 2014). The world's largest SMEs occur in association with the Great Oxidation Event (GOE, 2.42-2.31 Ga; Gumsley et al., 2017), but large SMEs persist throughout the geologic record and are broadly correlated with known fluctuations in Earth's redox balance (Figure 1; Maynard, 2010).

Manganese (II)-carbonates are the most common minerals in SMEs, occurring primarily as rhodochrosite ($MnCO_3$), with lesser amounts of the dolomite group mineral kutnohorite ($CaMn[CO_3]_2$) and Mn-enriched calcite (Maynard, 2010; Johnson et al., 2016). These carbonates consistently bear negative carbon isotope signatures (e.g. Tsikos et al., 2010; Johnson et al., 2013), which are conventionally viewed to indicate diagenetic reduction (via microbial dissimilatory respiration) of precursor Mn(III/IV)-oxides in sediment porewater (Calvert and Pederson, 1996).

While this diagenetic pathway for Mn-carbonate genesis is favored by most recent investigators, the implication of precursor Mn-oxides can be controversial. Johnson et al. (2013) proposed that a 2.42 Ga SME originated from Mn-oxides formed by a hypothetical Mn-oxidizing photoautotroph. However, these SMEs have alternatively been viewed as evidence for O_2 accumulation prior to, or at the onset, of the GOE (e.g. Ossa Ossa et al., 2018), or direct deposition of Mn-carbonates from a stratified water column (Herndon et al., 2018). Archean SMEs are particularly problematic to explain, but may represent the emergence of oxygen oases prior to the GOE (e.g. Planavsky et al., 2014), direct precipitation of Mn-carbonates from seawater (Farquhar et al., 2014), or Mn-oxidation by a consortia of anoxygenic phototrophs (Daye et al., 2019)

Although less commonly invoked in recent interpretations of SMEs, alternative pathways for Mn-carbonate genesis are feasible in the low-O_2 settings observed in modern redox-stratified environments (Force and Cannon, 1988). These include anaerobic metabolisms that generate dissolved inorganic carbon (DIC), increases in pH that favor carbonate saturation (Rincon-Tomas et al., 2016), or nucleation on Ca-carbonates (Herndon et al., 2018). Consistent with this view, Mn-carbonates have been observed in association with reducing conditions in redox-stratified lakes (Nuhfer et al., 1993; Stevens et al., 2000; Jones et al., 2011).

While many lines of evidence converge on the necessity for direct Mn-carbonate precipitation from redox-stratified water columns, few detailed evaluations of the processes governing this pathway are available, particularly from ferruginous analogs for Archean and Proterozoic marine settings (e.g. Crowe et al., 2011). This is exacerbated by the weak carbonate saturation of modern ferruginous lakes (the main analogs for ancient ferruginous oceans) relative to marine environments.

In this work we investigate a recently described ferruginous meromictic lake (Brownie Lake in Minnesota USA), which hosts both high dissolved Mn concentrations (up to 130 μM) and supersaturation of key carbonate phases, to assess Mn-mineralization pathways of relevance to anoxic environments across geologic time. We utilize this setting to evaluate the hypothesis—most recently advanced by Herndon et al. (2018)—that Mn carbonates may nucleate in the water column of redox stratified lakes. Here we describe the biogeochemical reactions occurring under ferruginous conditions that drive Mn-carbonate precipitation, and constrain the oxygen concentrations under which these processes occur. We then use this framework to assess the potential for anoxic Mn-carbonate genesis in the rock record, and evaluate the range of processes which may contribute to the carbonate carbon isotope signatures of these deposits.

2. Study site and methods

Brownie Lake (BL) is a small ferruginous lake located in Minnesota, USA. The general biogeochemistry of the site is described in Lambrecht et al. (2018), and Lambrecht et al. (2020) presented a detailed study of its methane (CH_4) cycle. Water column profiling, water sampling and analysis, and geochemical modeling were performed using routine techniques detailed these publications and in our Supplementary Materials.

To assess Mn-phases in the water column, we analyzed particulate material from water column filtration and sediment traps from intervals representing a transition from oxic (shallower) to anoxic (deeper) conditions. Particulates were collected on 0.2 μM filters in August 2018 from 4.5, 7, and 10 m depth. Water column sediment traps (at 3.5, 5, and 11 m depth) were deployed from June through October 2018. Surface sediment samples were also collected in August 2018. Particulate and sediment samples were processed anaerobically as detailed in Supplementary Materials.

Particulate and sediment samples were freeze-dried and Mn was extracted from 50-100 mg of material using 10 mL of 0.5 M HCl for 1 hour, which targets reactive Mn^{2+} and some Fe (Thamdrup et al., 1994; Supplementary Materials). Manganese in the extractants, as well as total Mn and Al from sediment traps and surface sediments, were quantified by Atomic Absorption Spectrometry (Thermo Scientific iCE3000 series), with an RSD of less than 2.1% for all measurements. Sediment trap and surface sediment samples were further analyzed by X-ray diffraction (XRD), as detailed in Supplementary Materials.

To assess the relationships between carbonate phases and water column conditions, we developed scenarios in Geochemist's Workbench (GWB) utilizing BL water chemistry from the depths that displayed the greatest degree of Mn-carbonate saturation (May 2017 at 6 m; July 2017 at 5.5 and 6 m). At these intervals we considered a range of inorganic and biological processes that have previously been suggested to occur at a ferruginous chemocline, including phototrophy, methanotrophy, sulfate (SO_4^{2-}) reduction, and Ca-carbonate dissolution. A full description of our modeling approach can be found in Supplementary Materials.

3. Results

3.1 Manganese and carbon cycling in ferruginous Brownie Lake

Multi-year water column monitoring of BL demonstrates a stable, redox-stratified, ferruginous water column, with a chemocline depth (steep concentration gradient of water column solutes) of 4.5 m and a maximum depth of 14 m (Lambrecht et al., 2018; Figure 2). Dissolved O_2 concentrations were as high as 402 µM at 1 m depth in April 2017, while values below detection (~3 µM) were reached at depths of 3.5 m in July 2017 and 5 m in October 2015 (Figure 2 a). Concentrations of dissolved Fe, Mn, and SO_4^{2-} follow trends observed in many redox stratified environments (Figure 2 b-d), with dissolved Mn (interpreted as Mn^{2+}) first increasing at the chemocline to a maximum concentration of 134 µM at 4.5 m in October 2015. Sulfate was present above the chemocline, with a maximum concentration of 377 µM at 4 m in October 2015 (not plotted); samples collected in later visits reached a maximum of 122 µM at 2 m in April 2017, but were more typically between 20-40 µM above the chemocline in 2017. Sulfide concentrations were more variable, with a maximum value of 74 µM recorded at 5 m in September 2017. Dissolved Fe (interpreted as Fe^{2+}) consistently accumulated below the zones of dissolved Mn maxima and SO_4^{2-} drawdown, and rapidly increased below 6 m, with a maximum value of 1430 µM at 13 m recorded in July 2017.

The concentration of DIC ranged from 1.62 mM in surface waters to 14.05 mM at depth, and generally followed the same pattern of increasing concentration with depth regardless of the date measured (Figure 2 e). The $\delta^{13}C_{DIC}$ ranged from -12.87‰ (5 m depth, September 2017) to a maximum of -1.97‰ at 12 m depth in May 2017. Regardless of the date visited, the lowest $\delta^{13}C_{DIC}$ values were found near the chemocline, with highest values at depth, and intermediate values in surface water (Figure 2 f).

Dissolved CH_4 concentrations were low near the surface (minimum 2.4 μM at 1 m depth April 2017) and increased to 1555 μM at depth (12 m, September 2017). Dissolved $\delta^{13}C_{CH4}$ ranged from -64.81‰ (5 m depth, September 2017) to values as high as -21.32‰ (4.5 m in May 2017; Figure 2 h inset). The $\delta^{13}C_{CH4}$ remained between -60 and -64‰ below the chemocline, and increased as dissolved CH_4 concentrations decreased (Lambrecht et al., 2020).

3.2 Brownie Lake pH and mineral solubility

Profiles for pH in 2017 (Figure 3 a) demonstrate features consistent with stratification, as well as seasonal changes. Surface water pH was generally higher than in deep water, rising as high as 8.85 in May 2017. Lowest pH values were observed below the chemocline late in the summer, with values as low as 6.26 observed in September 2017. The pH decrease across the chemocline was smaller in summer months, as demonstrated by the nearly identical pH profiles in May and July.

Surface water samples showed slight calcite supersaturation (Figure 3 b, maximum SI = 0.69 in April 2017; SI = saturation index or Q/K where Q = ion activity product, and K = given mineral solubility constant), with undersaturation observed in deeper waters (SI = -1.12 at 9 m depth in September 2017). Below the chemocline the Mn-carbonate phases pseudokutnahorite (max SI = 3.48 at 6 m depth, July 2017) and rhodochrosite (max SI = 0.46 at 6 m depth, July 2017) became supersaturated (Figure 3 c). As DIC and Fe^{2+} accumulated in the deepest waters, siderite ($FeCO_3$) also became supersaturated, with a maximum SI of 1.58 observed at 13 m in July 2017 (Figure 3 b). A closer examination of the key carbonate phases across the 2017 sampling dates (Figure 3 c) suggests that Mn-carbonate saturation varied throughout the summer, while calcite and siderite remained saturated in surface and deep waters, respectively.

Major Fe and Mn oxide phases were supersaturated in surface waters but became strongly undersaturated in anoxic waters (Lambrecht et al., 2018). The solubility of phosphate phases in BL is discussed in Supplementary Materials.

3.3 Particulate and sediment geochemistry

Figure 4 displays solid phase Mn data and carbonate mineralogy from three sources in BL: filtered particulates, sediment traps, and surface sediments. The HCl-extractable Mn fraction ranged from 862 ppm from the 3.5 m sediment trap, to 189 ppm from a particulate sample filtered from 10 m depth. The ratio of HCl-extractable Mn to total Mn in sediment trap and surface sediment samples ranged from 0.070 to 0.085, while total Mn/Al in these samples ranged from 0.021 to 0.032, with the highest values in both measures deriving from the 3.5 m sediment trap sample (Figure 4). Sediment trap materials from 5 m displayed more intense XRD peaks for calcite than did surface sediments.

3.4 Geochemical modeling

A process sensitivity analysis and results of simulations for three Mn-carbonate saturated BL intervals are shown in Figure 5, with model inputs shown in Table 1. After considering a broader range of potential processes that might influence carbonate saturation at a ferruginous chemocline (Supplementary Materials), we identified key relationships in the sensitivity analysis for the July 2017 5.5 m interval (the most strongly Mn-carbonate supersaturated in our study) that governed the carbonate saturation behavior of all of our simulations. The first two simulations assessed the role of aerobic organic carbon respiration (AR) versus aerobic CH_4 oxidation (MO):

(1) $CH_2O + O_2 = CO_2 + H_2O$ (AR)

(2) $CH_4 + 2O_2 = CO_2 + 2H_2O$ (MO)

The key difference between the two processes is the molar ratio of O_2 consumed to CO_2 produced: 1:1 for AR, and 2:1 for MO. Both scenarios had the same impact on carbonate saturation. The greater impact of these processes was the removal of O_2, which even at the very low concentrations observed in the upper chemocline of BL appears to inhibit Fe^{2+} activity in the model. Complete O_2 removal enhanced Fe^{2+} activity and created a subtle boost in siderite saturation (+0.4 Q/K) in both scenarios, with no other observable differences.

Next we considered sulfate reduction (SR), which adds 2 moles of HCO_3^- for each mole of SO_4^{2-} consumed.

(3) $SO_4^{2-} + 2CH_2O = H_2S + 2HCO_3^-$ (SR)

Sulfate reduction had a subtle impact on carbonate saturation, with siderite showing the greatest increase (~0.6 Q/K), followed by rhodochrosite (~0.2 Q/K) then calcite; the greatest changes occurred in the first two days of the simulation.

Next we assessed the addition of calcite at a rate consistent with surface water calcite saturation from July 2017 (Supplementary Materials). Calcite addition had the greatest impact on rhodochrosite solubility during the simulation, increasing it by 1.5 Q/K. Calcite solubility had a more subtle response, increasing by only 0.5 Q/K, while siderite solubility experienced no change in this scenario.

The remaining panels in Figure 5 display the impact of the combined processes (MO, SR, and calcite addition) with varying temperature and pH. Increasing temperature in the system to 25°C resulted in modest increases in mineral saturation, though the relative changes are the same for each mineral. Increasing the system pH from 7 to 8.5 resulted in significant increases in mineral saturation, particularly between pH 7.5 and 8. At the highest pH (8.5), siderite experienced nearly the same increase in Q/K as rhodochrosite.

A final series of scenarios (Figure 5 i-l) considered a solution based on BL dissolved Fe, Mn, O_2, and SO_4 values, and adopting modern seawater concentrations for the remaining ions at pH 8 and a temperature of 25°C. In the first scenario with dissolved Mn concentration from the BL July 5.5 m interval (Figure 5 i), calcite saturation increased more than rhodochrosite. However, increasing dissolved Mn concentration in subsequent seawater scenarios led to significant increases in rhodochrosite Q/K (~+15), with the maximum observed increase corresponding to a Ca:Mn of 18, which was the highest observed in BL.

Figure 6 shows the impacts of combined SR, MO, and calcite addition on carbonate mineral saturation from three BL intervals: May 2017 at 6 m, and July 2017 at 5.5 and 6 m, as detailed in Table 1. The results are shown for both mineral precipitation suppressed (as delta Q/K) and unsuppressed (μmol precipitated) scenarios, as well as the response in system pH through the course of each simulation.

In each suppressed scenario (Figure 6 a-c) rhodochrosite saturation increased the most, followed by siderite, while calcite saturation increased linearly throughout the simulation. Siderite saturation displayed a similar pattern in each scenario, with an initial sharp increase followed by a more gradual climb, and siderite saturation increased nearly as much as rhodochrosite in the July 2017 6 m scenario (Figure 6 b). In these scenarios pH gradually increased in each case (Figure 6 d-f)

Unsuppressed scenarios demonstrated key differences in the proportions of minerals produced by these simulations (Figure 6 g-i). One scenario created more calcite than rhodochrosite, the second created a mixture of the three minerals, and the last precipitated only rhodochrosite. In unsuppressed scenarios, pH changes were generally more muted (Figure 6 j-i), and system pH was lower overall.

4. Discussion

4.1 Manganese and carbonate cycling in Brownie Lake

Reactive particulate (HCl-extractable) Mn, representative of carbonate-associated Mn, was present in BL only below the seasonal oxycline (~3.5 m), and represented a consistent fraction of total anoxic sediment Mn (Figure 4 c.). Coupled with XRD evidence for calcite dissolution below the BL chemocline (Figure 4 d.), we suggest this phase most likely consists of calcite crystals precipitated in surface waters, which became encrusted with Mn-enriched rims during water column settling, resulting in crystals similar to those previously documented in lake sediments (Stevens et al., 2000; Herndon et al., 2018).

Although we cannot eliminate the possibility that some HCl-extractable Mn in BL was associated with a non-carbonate phase, such as a poorly crystalline sulfide or phosphate (see discussion in Supplementary Materials), it is unlikely to represent Mn-oxides. Mn-oxides are thermodynamically unstable in ferruginous BL as their reduction is rapidly coupled to the oxidation of Fe(II), sulfide, ammonium and CH_4 (e.g. Jones et al., 2011), all of which are present in BL waters (Lambrecht et al. 2018; Figure 2). Furthermore, while HCl-extractable Mn was associated with Mn-oxide phases in ferruginous Lake Matano, this was for samples containing nm-scale oxide filaments above the chemocline. By contrast, below the Matano chemocline Mn-oxides were rapidly reduced and replaced by a phase with a XANES spectrum consistent with rhodochrosite (Jones et al., 2011).

The dissolved Mn accumulation in the BL chemocline is among the most concentrated reported in redox-stratified lakes (up to 134 μM), indicating the presence of a vigorous Mn redox cycle (e.g. Jones et al., 2011; Herndon et al. 2018). Microbial Mn^{2+} oxidation may contribute to Mn cycling within the BL chemocline, where it is known to operate efficiently within the O_2 concentration gradients (~3-30 μM) observed there (Clement et al., 2009). Seasonal dynamics of the BL Fe and S cycles may also contribute to the dissolved Mn pool, as late season sulfide generation by SR drives removal of dissolved Fe, increasing dissolved Mn:Fe at the top of the chemocline.

Water column pH decreased with depth but stabilized at the chemocline before reaching its lowest values in the deepest waters (Figure 3). This zone of pH stability at the chemocline was likely driven by a number of processes buffering the overall decline in pH with depth. For example, Mn-oxide reduction raises pH when coupled to organic carbon, sulfide, or CH_4 oxidation (Jones et al., 2011; Johnson et al., 2013):

(4) $CH_2O + 2MnO_2 + 2H^+ = CO_3^{2-} + 2Mn^{2+} + 2H_2O$

(5) $H_2S + 4MnO_2 + 2H_2O = SO_4^{2-} + 4Mn^{2+} + 6OH^-$

(6) $CH_4 + 4MnO_2 + 7H^+ = HCO_3^- + 4Mn^{2+} + 5H_2O$

Of these processes, we consider reactions 4 and 5 most likely to be active at the BL chemocline, based on the concentrations of species present and the eutrophic nature of the lake (Lambrecht et al., 2020), which provides a large reservoir of organic carbon to the system. Similar to reaction 4, iron reduction coupled to organic carbon oxidation is also capable of decreasing acidity (Walter et al., 2014). While experiments confirm that reaction 6 can be microbially mediated (Ettwig et al., 2016), organisms putatively capable of such a reaction were in very low abundance (Lambrecht et al., 2020), and reaction thermodynamics seem unlikely to support such organisms in BL.

Pelagic calcite dissolution, a well-known processes in seasonally stratified lakes (e.g. Myrbo and Shapley, 2006), may further serve to influence pH and DIC changes at the chemocline, via:

(7) $CaCO_3 + H^+ = Ca^{2+} + HCO_3^-$

or by uptake of CO_2 released through reactions 1 and 2:

(8) $CaCO_3 + CO_2 + H_2O = Ca^{2+} + 2HCO_3^-$

Our solubility calculations (Figure 3), the reduction in intensity of the calcite XRD peaks between the sediment trap and surface sediments (Figure 4), and the enrichment in dissolved Ca in the deep waters of BL (Lambrecht et al., 2018), are all consistent with calcite dissolution occurring near the chemocline.

Surface levels of BL carbonate saturation and changes across the chemocline are similar to those recently documented in euxinic Green Lake, NY (Herndon et al., 2018), but key differences emerge in the deep ferruginous waters of BL. In Green Lake, rhodochrosite was only supersaturated in a narrow zone around the chemocline. In BL, rhodochrosite was supersaturated at and below the chemocline, and siderite became supersaturated in deep ferruginous waters. This would enable continued Mn-carbonate crystal growth in deep water, with potential for incorporating Fe into carbonates where bottom waters are saturated in siderite.

Carbonate crystals likely spend sufficient time in Mn-enriched waters to incorporate significant Mn^{2+}. Stokes settling times (at 25° C) for 5 μm crystals through a non-turbulent, 1.5 m chemocline are on the order of several hours, and increase exponentially for smaller crystals. Experimental studies (e.g. Pingitore et al., 1988) suggest Mn^{2+} uptake by calcite is favored at slower precipitation rates that would nonetheless generate significant amounts of Mn-carbonates at these settling velocities (e.g. 200 $\mu g\ min^{-1}\ m^{-2}$). Hence Mn-carbonate precipitation would be favored in an environment where μm-scale crystals settle for several hours or more, and remain in contact with rhodochrosite supersaturated waters at the sediment-water interface, as is observed in BL (Figure 3).

4.2 Controls on carbonate solubility in Brownie Lake

Our sensitivity analysis demonstrates that calcite addition has the greatest impact on rhodochrosite saturation in BL (Figure 5). This is likely driven by the relative solubilities of the two minerals, with more soluble calcite (pK = 8.48 vs. rhodochrosite pK = 10.08, Morse et al., 2007) dissolving at the chemocline and contributing bicarbonate to the system (eq. 8). The sensitivity of the system to increases in rhodochrosite saturation appears to be further governed by increasing dissolved Mn concentration (up to 400 μM), pH, and temperature. As Fe concentrations increase, such as below the chemocline, siderite becomes an significant component of the system.

Sulfate reduction at the BL chemocline also holds the potential to influence carbonate saturation. Despite generally low SO_4^{2-} concentrations, SR is active in BL waters, consistent with other ferruginous lakes where vigorous sulfur cycling occurs (Walter et al., 2014). Because SR generates two mol of HCO_3^- for each mol of SO_4^{2-} reduced (eg. 3), this process drove an initial spike in Fe-Mn carbonate saturation in our modeled intervals (e.g. Figure 5 c).

Unsuppressed scenarios (Figure 6) show that subtle variations in water Mn:Fe and pH can produce carbonate assemblages with highly variable proportions of Ca-Mn-Fe, consistent with many ancient examples of Mn enrichments where both Mn-Ca and Mn-Fe carbonates are reported (Tsikos et al., 2010; Johnson et al., 2016; Planavsky et al. 2018). Although the assumption of siderite precipitation at 1-fold saturation may be unrealistic in these scenarios, nucleation on existing crystals may lower the kinetic barriers to precipitation relative to homogeneous phases (Jiang and Tosca, 2019). Experimental work previously implicated calcite as a catalyst in Mn-carbonate precipitation. Mucci (2004) suggested Mn-carbonate minerals could nucleate on small calcite crystals, or manifest as manganoan rims on calcite if concentrations of Ca^{2+} were much greater than Mn^{2+}.

These scenarios translated well to manganiferous seawater with minor adjustments. Increasing temperature and pH favored carbonate production (Figure 5 e-h), but an initial seawater scenario (Figure 5 i) illuminated a challenge to the model: competition between calcite and rhodochrosite at marine concentrations of Ca. The molar Ca:Mn of BL water in our sensitivity scenarios derives from a measured value of 25.6, but scaling to marine Ca increases this ratio to 138 (Table 1). Adjusting the dissolved Mn concentration of the seawater scenarios to include the highest measured concentration observed in this study (134 μM) led to greater increases in rhodochrosite saturation, consistent with BL scenarios. Subsequent seawater scenarios with 200 μM dissolved Mn, and a Ca:Mn ratio adjusted to the lowest observed in BL (~18 or a dissolved Mn concentration of 571 μM) generated considerable increases in rhodochrosite saturation relative to calcite, demonstrating the viability of this mechanism in marine settings. Although the final scenario had a dissolved Mn concentration over 4-fold larger than we observed in BL, it is not an unreasonably high concentration for a marine system given the dissolved Mn concentrations of >400 μM reported in the modern Orca Basin (Van Cappellen et al., 1998).

4.3 Dissolved inorganic carbon isotopes in redox-stratified waters

Differences in $\delta^{13}C_{DIC}$ behavior between euxinic versus ferruginous waters largely derive from the prominence of the CH_4 cycle in ferruginous systems. Although modern ferruginous lakes occur in a variety of hydroclimatic settings, data presented here (Figure 2) reinforce the observation that these systems display stratification in $\delta^{13}C_{DIC}$.

Ferruginous chemoclines host lower $\delta^{13}C_{DIC}$ relative to deep waters that are influenced by fermentation or methanogenic CO_2 reduction (Assayag et al., 2008; Crowe et al., 2011; Lambrecht et al. 2020; Figure 2). Calcite dissolution also holds potential to contribute heavier DIC to deep waters (Myrbo and Shapley, 2006). In contrast, euxinic lakes also demonstrate a more common mode of $\delta^{13}C_{DIC}$ stratification, wherein waters from the chemocline and below reflect light $\delta^{13}C_{DIC}$ release from AR and SR of organic carbon (Myrbo and Shapley, 2006; Havig et al., 2017; Figure 7).

4.3.1 Impact of methane oxidation on Brownie Lake DIC

A pronounced depletion in $\delta^{13}C_{DIC}$ at the chemocline and progressive enrichment through deep anoxic waters reflect active CH_4 cycling in the BL water column, with oxidation at the chemocline, and methanogenesis in deep anoxic waters (Lambrecht et al., 2020; Figure 2 e & f). The increase towards positive $\delta^{13}C$-CH_4 consistent with methanotrophy occurs at the base of the oxycline, at O_2 concentrations between 4-5 μM. While SO_4-dependent anaerobic oxidation of CH_4 (AOM) is marginally thermodynamically permissible in this context, BL 16S rRNA sequencing recovered negligible sequences of putative AOM archaea (Lambrecht et al., 2020). This is consistent with recent work demonstrating that aerobic methanotrophy remains favored in ferruginous systems even at oxygen levels below the detection limit of most sensors (~ 20 nmol; Oswald et al., 2016).

Both SR and MO are thermodynamically favored in BL (Supplementary Materials), and capable of influencing $\delta^{13}C_{DIC}$. It is therefore necessary to consider which process may be exerting a greater influence on BL DIC. Employing the reaction-diffusion approach developed by Crowe et al. (2011), and adopting the vertical eddy diffusivity value around the chemocline of BL on the order of 5x10^{-5} m^2/s (Lambrecht et al., 2018), we calculate that an MO rate of 160 µmol/L/day is required to maintain the negative DIC carbon isotope excursion observed at 4.5 m depth in September 2017. This is within the range of known lacustrine MO rates, and slightly higher than the maximum rate recently determined in ferruginous Lake Matano (Sturm et al., 2019). Although dissolved oxygen concentrations at this interval (~4.7 µM) were just above the detection limit of our sonde (2-3 µM), they would be sufficient to maintain aerobic CH_4 oxidation. This rate is also similar to the upward flux of CH_4 towards the chemocline, as calculated from the CH_4 concentration profile (90 µmol/L/day, assuming oxidation occurs over a 0.5 m interval), suggesting that the BL carbon isotope excursion could be maintained primarily by MO, though contributions to the pool of isotopically light DIC from other pathways is further evaluated below.

A mass balance of BL DIC data suggests MO has a stronger influence on the DIC excursion at the chemocline, with a ratio of ~3:1 MO:SR, consistent with its thermodynamic favorability (Supplementary Materials). Nitrate- and Fe-Mn-coupled AOM (Ettwig et al., 2016; Oswald et al., 2016) are intriguing but remote possibilities, considering such organisms were not significant in BL (Lambrecht et al. 2020). Concentrations of NO_3^- observed at Brownie Lake are generally <2 µM (Lambrecht et al., 2018) and are not likely to significantly impact the CH_4 budget. And although it has been demonstrated in experiments (Ettwig et al., 2016), a clear example of pelagic MO coupled to Fe/Mn oxide reduction has yet to be produced. Thus, this analysis suggests that aerobic CH_4 oxidation may exert a major influence on $\delta^{13}C_{DIC}$ in Brownie Lake, consistent with the suggestion that methanotrophy is a major influence on $\delta^{13}C_{DIC}$ in ferruginous waters (Crowe et al., 2011).

4.3.2 Methane oxidation and carbonate C isotopes

The widespread observation of low $\delta^{13}C$ in Mn-carbonates is traditionally interpreted as evidence of diagenetic oxide reduction coupled to organic carbon respiration within sediments (e.g. Calvert and Pederson, 1996; Planavsky et al., 2018). While this interpretation is viable in many geological examples, the influence of MO and SR on $\delta^{13}C_{DIC}$ in ferruginous lakes demonstrates the potential for embedding signatures of these processes in primary carbonate minerals.

Carbonates derived from CH_4 oxidation have long been recognized (Michaelis et al., 2002) and are widely described in modern lacustrine and marine environments. In marine settings, SO_4-AOM triggers precipitation of carbonates and sulfides (Michaelis et al., 2002). In completely anoxic and ferruginous settings where SO_4^{2-} is below 10s of μM, benthic archaea have been shown to couple both Fe and Mn-oxide reduction to CH_4 oxidation (Ettwig et al., 2016), a reaction that similarly favors carbonate precipitation (Crowe et al., 2011).

Aerobic oxidation of CH_4 to CO_2 has a substantially lower redox potential relative to Mn^{2+} oxidation, permitting CH_4 oxidation in suboxic environments where Mn^{2+} would remain reduced (Supplementary Materials). Such a nuanced separation of these processes is possible in a redox-stratified water column, but would be less likely to overlap in sediments where oxygen would be unlikely to penetrate to a zone of methane production.

Earlier interpretations of $\delta^{13}C$ from iron formation carbonates suggested greater variability in the $\delta^{13}C$ of marine DIC sources (e.g. Winter and Knauth, 1992), consistent with the recent suggestion that signatures of hydrothermal DIC may be recorded by some ancient Fe-carbonates (Jiang and Tosca, 2019). Although the interpretation of primary versus diagenetic signatures of ancient carbonates remains subject to much debate, it is clear that a number of primary processes operating in redox-stratified water columns may generate substantial variability in $\delta^{13}C_{DIC}$.

4.4 Mn-carbonates in anoxic environments

Recent literature largely assumes that Mn burial in permanently anoxic basins is not permissible due to the instability of Mn-oxides and high solubility of Mn-sulfides (Calvert and Pederson, 1996). In the prevailing view, Mn-carbonates form in sediment porewater after diagenetic reduction of Mn-oxides precipitated from water columns that are at least episodically oxidized (e.g. Johnson et al., 2013). Our findings, however, are consistent with work in both ferruginous (Jones et al., 2011) and euxinic lakes (Herndon et al., 2018), supporting the hypothesis that primary precipitation of Mn-carbonates is favorable in redox-stratified water columns containing 5 μM of oxygen or less.

Observations of Mn-carbonates in sediment traps (Nuhfer et al., 1993), water column particulates (Jones et al., 2011), and Holocene sediments (Wittkop et al., 2014) from redox-stratified lakes further support the existence of a primary precipitation pathway. The Mn-carbonate phase documented in Elk Lake, Minnesota was not found in sediment traps sterilized with formalin (Nuhfer et al., 1993), implicating microbial processes in its precipitation (Stevens et al., 2000). Consistent with marine examples, the lacustrine Mn-carbonate overgrowths on calcite crystals documented by Stevens et al. (2000) corresponded to lighter bulk carbonate $\delta^{13}C$ than in intervals without Mn-carbonates, consistent with a potential role for AR or MO in their origin.

This evidence also points to a relatively rapid precipitation of Mn-carbonates within redox-stratified water columns. Rhodochrosite was identified by XRD in sediment traps by Nuhfer et al. (1993), and in particulate samples by XANES in Lake Matano (Jones et al., 2011). Pseudokutnohorite is thermodynamically favored to precipitate before rhodochrosite (Mucci 2004), but to our knowledge this XRD-amorphous mineral has not been reported in lacustrine settings, though Stevens et al. (2000) reported kutnohorite in Holocene sediments.

4.5 Application to ancient SMEs

In light of the evidence presented here, we advance a primary carbonate model for the genesis of SMEs (Figure 7 a). The key elements of the carbonate model are, 1) a redox stratified basin hosting Mn-enriched waters near a redoxcline, 2) Ca-carbonate precipitation in shallow waters, and 3) a lysocline poised near the basin redoxcline. While our work demonstrates that this model may be especially viable in ferruginous environments, it is also consistent with suggestions that Mn-carbonates may represent an primary precipitate in euxinic settings (Force and Cannon, 1988; Herndon et al., 2018).

Most SMEs occur in shallow water facies (Force and Cannon, 1988), and secondary enrichment is precluded in key examples (e.g. Johnson et al., 2013), thus their genesis requires the presence of Mn-enriched waters in shallow marine environments, and hence a shallow chemocline. Substantial deposits require proximity to hydrothermal Mn sources (Maynard, 2010), which may dictate the Mn:Fe of basin waters, but additional Fe and Mn segregation may occur at a chemocline as observed in BL. Fe can be oxidized by anoxygenic photoferrotrophy in the photic zone (e.g. Lliros et al., 2015), or by microaerophilic Fe(II)-oxidizing bacteria (Berg et al., 2019). Both of these processes would increase dissolved Mn:Fe. A cryptic sulfur cycle may similarly proceed under weakly oxidizing conditions (e.g. Walter et al., 2014), leading to an increase in Mn:Fe via Fe-sulfide precipitation (Force and Cannon, 1988).

In contrast to the episodic mixing observed in seasonally-stratified lakes, a more stable marine environment would offer the advantage of maintaining the redox relationships observed in BL for longer periods of time, enhancing the potential for large-scale Mn mineralization. Basin upwelling events may introduce Mn-enriched waters to depositional sites, but many SMEs are also linked to marine transgressions (Roy, 2006). A transgression could lead to migration of a chemocline over previously deposited Ca-carbonates, where Mn-enriched waters would have the opportunity to act as a “mineralizing fluid” on surface sediments (Force and Cannon, 1988). Changes in sea level may also lead to interbedding of primary carbonates alongside Mn-oxides, which could later be diagenetically reduced, accounting for the complex mineral associations observed in major Mn enrichments (e.g. Johnson et al., 2016). Independent of eustatic sea level, the chemocline may shift position in response to the relative supply of oxidants versus reductants in seawater (e.g. Lantink et al. 2018).

Capture of Mn by carbonate phases may preclude large-scale oxide precipitation if the rate of carbonate capture and burial equals or exceeds the rate of Mn supply to the basin. In contrast, a large Mn-oxide deposit would indicate a rate of Mn upwelling and oxidation exceeding the rate of capture by carbonates, or a transition to an environment unfavorable for carbonate production or preservation.

4.5.3 The carbonate pathway in Precambrian SMEs

Sharp facies gradients between Ca-carbonates and ferruginous or manganiferous sediments are present in many examples SMEs occurring both before and after the GOE (e.g. Johnson et al., 2013; Lantink et al., 2018; Ossa Ossa et al., 2018b), implying the presence of a basin lysocline. The lysocline in small temperate lakes such as BL is driven primarily by temperature and rates of OM remineralization (e.g. Myrbo and Shapley, 2006). In ancient ferruginous basins, a shallow lysocline may have been further supported by the presence of metal-enriched hydrothermal waters with a lower pH relative to surface waters.

Recent estimates of dissolved O_2 concentrations derived from Archean SMEs are higher than the 3-4 µM we considered in our BL simulations, but are generally consistent with the 3-30 µM range we observe in manganiferous BL waters. The concentrations of dissolved O_2 represented by Archean SME may have locally exceeded 10 µM (Ossa Ossa et al., 2018), within a range that could support rapid microbial Mn^{2+} oxidation and further concentrate dissolved Mn at a local chemocline (Clement et al., 2009).

Although Mn-oxides may be generated in some low-O_2 settings (e.g. Daye et al. 2019), the relationships between O_2 and manganiferous waters in BL imply that efficient Mn-oxide burial would require O_2 concentrations at the sediment water interface to remain significantly above 5 μM. We observed O_2 concentrations ranging between ~5-50 μM at the top of the BL chemocline where tens of μM of dissolved Mn began to accumulate, indicating Mn-oxide reduction was occurring in these waters. Hence Mn would remain dissolved in environments where O_2 may be present at <5μM—concentrations that could nonetheless support Fe^{2+} and CH_4 oxidation. Here a carbonate burial pathway for Mn^{2+} would remain viable, with the production of various Mn-minerals dependent on reaction kinetics and the stability of redox gradients.

These interpretations are consistent with Fe-isotope evidence from the Hotazel Formation of the Transvaal Supergroup, deposited near the onset of the GOE. Hotazel records suggest SME genesis from a redox-stratified basin possessing a large reservoir of dissolved Fe, and evolving Fe-Mn ratios (Lantink et al. 2018). A primary carbonate model also accounts for the co-occurrence of Mn(II-III) and Fe(III) phases in Mn-enrichments interpreted to represent a limited role for diagenetic reduction in the genesis of Hotazel SMEs (Tsikos et al., 2010).

Manganese enrichments in deep water facies of the Proterozoic Animikie Basin were recently interpreted as evidence of complete water column oxidation (Planavsky et al. 2018), who invoked a Baltic Sea analog (e.g. Hausler et al., 2018). While the Baltic Sea SMEs are consistent with deep water oxygenation and genesis from Mn-oxide precursors, they also occur in an environment of very low Fe:Mn, which is not consistent with the high Fe:Mn of the manganosiderite phases preserved in the Animikie examples (Planavsky et al, 2018). A primary carbonate genesis of the Animikie examples followed by continued Fe-carbonate growth on the seafloor (e.g. Figure 7 a.) is more consistent with both previous work on the Animikie Basin (Poulton et al., 2010), and examples of highly Mn-enriched Fe-carbonates preserved in ferruginous Holocene sediments (Wittkop et al., 2014).

Although Mo isotope depletions are frequently interpreted as indicators of Mn-oxide burial (e.g. Planavsky et al., 2018), they may also occur at a euxinic chemocline in association with changes in Mo-S speciation (Neubert et al., 2008). The co-occurrence of pyrite with Proterozoic SMEs (Johnson et al., 2013; Planavsky et al., 2018) supports this view, and opens the possibility that some Precambrian SMEs contain records of cryptic S cycling as opposed to complete water column oxidation.

4.5.4 The carbonate pathway in Phanerozoic SMEs

Manganese enrichments from the Neoproterozoic and younger are generally consistent with more diverse mineralization pathways relative to older examples (Maynard, 2010). Phanerozoic SMEs are frequently associated with black shales, whose sulfides represent an effective Fe-sink, allowing for accumulation of dissolved Mn in the water column (Force and Cannon, 1988). These younger SMEs may remain associated with large-scale changes in marine redox balance, including ocean anoxic events, and the occurrence of marine red-beds, which have recently been interpreted as evidence for transient ferruginous episodes in the Phanerozoic (Figure 1; Song et al., 2017). Localized tectonic influences may overprint this global signal, which is the likely case for the Oligocene deposits associated with the Black Sea (Force and Cannon, 1988).

The Jurassic Molgano deposit of Mexico is the largest Phanerozoic SME, occurring at the base of a Ca-carbonate facies (Okita, 1992), where it is tellingly not associated with primary oxides (Force and Cannon, 1988). Instead, detailed mapping of Mn-phases in Molgano samples suggests manganoan calcite may have represented the earliest precipitate (Johnson et al., 2016). Other Phanerozoic examples including the Oligocene Nikopol deposit of Ukraine and Cretaceous Groote Eylandyt deposit of Australia contain Mn-carbonates associated with primary oxides. This co-occurrence of adjacent oxide and carbonate SMEs within the same sedimentary basin likely represents the preservation of a water column redox boundary (Force and Cannon, 1988). Careful re-assessment of such Phanerozoic SMEs utilizing new paleoredox tools is likely to provide insight into their relationships with global versus localized drivers of their genesis.

5. Conclusions

We document the production and burial of an HCl-extractable particulate Mn phase, interpreted as a Ca-Mn-carbonate, from a ferruginous Brownie Lake. Geochemical models of carbonate production in the lake suggest introduction of calcite to Mn-rich waters at the chemocline triggers substantial increases in rhodochrosite saturation. These models translate to ferruginous marine conditions, implying a significantly less oxidizing environment is required to develop carbonate-hosted sedimentary Mn enrichments than previously recognized. Specifically, our findings suggest primary Mn-carbonates may originate from waters containing 5 μM dissolved O_2 or less, and do not require the burial of precursor Mn-oxides in sediments.

Instead of representing diagenetic organic carbon respiration, the negative carbon isotope composition commonly observed in Mn-carbonates might also be imparted by organic carbon remineralization or CH_4 oxidation occurring in the water column. Hence some sedimentary Mn enrichments may develop where processes operating in low O_2 environments including sulfur cycling, microaerophilic Fe-oxidation, or anoxygenic photosynthesis co-occur with a basin lysocline. This interpretation may reconcile inconsistencies among paleoredox proxies in environments where Mn-enriched sediments are encountered.

Acknowledgements

We thank Andrey Bekker, Louis Derry, Frantz Ossa Ossa, and an anonymous reviewer for suggestions that significantly improved this contribution. J. Barry Maynard generously shared his compilation of manganese ore data. This study was supported by an NSF awards (EAR-1660691, EAR-1660761, EAR-1660873) to ES, CW, and SK, and by NSF-1338322 to AM and others. ES's contribution benefited from support of the Iowa Space Grant Consortium under NASA Award No. NNX16AL88H. We thank Duncan

Widman, Paige Bauer, Raisa Islam, and Gabrielle Ledesma for field and laboratory assistance.

Figure and Table Captions

Figure 1: Sedimentary manganese enrichments (SMEs) through geologic time in comparison with redox indicators. Manganese data replotted from Maynard (2010), expressed as metric tons Mn metal, including sub-economic and iron-formation hosted deposits. a. Atmospheric O_2 from Lyons et al., 2014. b. All SMEs binned in 200 Myr increments. c. Post-Neoproterozoic marine redox indicators including ocean anoxic events (OAEs; stars) from Jenkyns (2010), and cumulative thickness of marine red beds (MRBs), replotted from Song et al. (2017). d. Post-Neoproterozoic SMEs binned in 25 Myr increments.

Figure 2: Brownie Lake 2015-2017 water column profiles of (a) O_2, (b) dissolved iron (Fe^{2+}), (c) dissolved manganese (Mn^{2+}), (d) SO_4^{2-} and total dissolved sulfide (ΣS^{2-}), (e) dissolved inorganic carbon (DIC), (f) the carbon isotopic composition of DIC, (g) dissolved methane (CH_4), and (h) the carbon isotopic composition of dissolved CH_4

(inset shows high values observed near the chemocline). Replotted from Lambrecht et al. (2020).

Figure 3: (a) pH, (b) calcite solubility, and (c) rhodochrosite (rhod.), and siderite (sid.). solubility in the Brownie Lake water column in 2017. (d) Detail of July 2017 phases including pseudokutnohorite (pseudokut.). Saturation index (SI) = log(IAP/K_{sp}) where IAP is the solution ion activity product and K_{sp} is the solubility constant of the given mineral.

Figure 4: Brownie Lake particulate and water column data from 2018. (a) Brownie Lake water column dissolved O_2 and Mn. (b) Concentrations of HCl-extractable Mn from filtered particulates, sediment trap materials, and surface sediments. (c) Sediment trap and surface sediment HCl-extractable Mn normalized to total Mn (Mn_T), and Mn/Al. (d) X-ray diffraction patterns from 5 m sediment trap sample versus surface sediments. Note the prominence of the calcite peak in the sediment trap at 5 m relative to surface sediments, interpreted as evidence of water column calcite dissolution. XRD peak labels: C = calcite, D = dolomite, F = feldspars, M = 2M muscovite, Q = quartz.

Figure 5: Sensitivity of BL carbonate mineral saturation. Cal = calcite (blue), Rhod = rhodochrosite (black), and Sid = siderite (red). All changes expressed in terms of delta Q/K where Q = IAP and K = given mineral solubility constant. All scenarios are plotted in terms of a 15-day simulation and based on BL water chemistry as measured in July 2017 at 5.5 m (Table 1). See main text for example reactions. (a.) Scenario considering

aerobic respiration where O_2 and CO_2 are reacted in a 1:1 molar ratio. (b.) Methane oxidation scenario where 2 moles of O_2 are consumed for every CO_2 produced. (c.) Sulfate reduction scenario. (d.) Addition of calcite at 7 μmol/day scenario. (e-h.) The combination of scenarios b-d. with varying temperature and pH. Note change in scale of delta Q/K for g. and h. (i-l.) Scenarios combining b-d. adopting Brownie Lake dissolved Fe, Mn, SO_4, and O_2 concentrations and assuming seawater composition and pH and temperature of 25 C. (i.) Seawater with Brownie Lake July 2107 5.5 m concentrations of Fe, Mn, SO_4 and O_2. (j.) Scenario as described in (i.) with dissolved Mn concentration increased to 134 μM, the highest observed in our study. (k.) Scenario as described in (i.) with dissolved Mn concentration increased to 200 μM. (l.) Scenario as described in (i.) with Ca:Mn ratio set to 18, the lowest observed in our study.

Figure 6. Combined scenarios for methane oxidation, sulfate reduction, and calcite addition (i.e. Figure 5 b-d) applied to rhodochrosite-saturated intervals in BL. Mineral abbreviations and Q/K relationships as in Figure 5. Panels a-c with mineral precipitation suppressed to assess changes in solubility. (a) May 2017 6 m, (b) July 2017 5.5 m, (c) July 2017 6 m. Panels d-f display pH changes from each of the scenarios above. Panels g-i display results from unsuppressed simulations where minerals are allowed to precipitate at Q/K = 1 and accumulate in the system, with mineral concentrations shown in μmoles. Panels j-l display pH evolution of unsuppressed scenarios g-i.

Figure 7: Models for the genesis of sediment manganese enrichments (SMEs). Relative water column composition of $\delta^{13}C_{DIC}$ and concentrations of O_2, Mn, Fe, and H_2S (if

applicable) shown to right. Each model assumes the presence of a basin lysocline coincident with a chemocline. Sources of Fe and Mn may include hydrothermal vents, springs (in lakes), or sediment porewater release. See main text for example reactions. (a) Carbonate model, based on the ferruginous setting described in this work. Manganese oxides may not be present if Mn-carbonate genesis rate exceeds rate of supply, and oxygenic photosynthesis may not have been active in earliest Archean examples. Calcite introduced to water column via littoral precipitation dissolves as it settles into the lysocline, where Mn-carbonates nucleate. Fe-rich overgrowths may precipitate (ppt) in deep waters if siderite saturation is exceeded. Fe-silicates such as greenalite may also co-precipitate in deep facies of Precambrian oceans (Jiang and Tosca, 2019). The composition of $\delta^{13}C_{DIC}$ is adopted from trends observed in Brownie Lake, but Precambrian oceans (pC) may not have hosted enriched $\delta^{13}C_{DIC}$ in deepest waters. Transgression is capable of shifting facies relationships to the left, creating contrasting sediment compositions. (b) Euxinic model, similar to the zoned model of Force and Cannon (1988) and a mechanism proposed by Herndon et al. (2018). Instead of carbonates, iron-sulfides dominate in deeper settings, but Mn-carbonates may still precipitate near the chemocline or if rates of $CaCO_3$ accumulation are high throughout the basin (e.g. Green Lake; Herndon et al., 2018). The $\delta^{13}C_{DIC}$ of deep water is shifted negative due to the predominance of sulfate reduction (Myrbo and Shapley, 2006). (c) The prevailing oxide model assumes that Mn-carbonates precipitate from a precursor oxide mineral (e.g. Calvert and Pederson, 1996). A deep water source of dissolved Mn is still implied. In Precambrian settings ferruginous conditions were likely dominant, but anoxic basins in the Phanerozoic are often interpreted as euxinic (H_2S rich). Both the carbonate and euxinic model may produce SMEs in suboxic environments, but low carbonate saturation or high rates of dissolved Mn upwelling may favor the oxide model.

Table 1: Inputs and reaction rates for carbonate modeling. Species concentrations (Conc.) were measured from the BL water column except the seawater scenario, which adopted values of major dissolved ion concentrations from seawater with the exception of Fe, Mn, SO_4, and O_2. The Mn concentration in the seawater scenario is based on the lowest observed BL Ca:Mn, with results shown in Figure 5 l. Reaction rates were determined by dividing the measured concentrations by 15 days, the length of the scenario.

References Cited (50/50)

Assayag, N., Jézéquel, D., Ader, M., Viollier, E., Michard, G., Prévot, F., and Agrinier, P., 2008. Hydrological budget, carbon sources and biogeochemical processes in Lac Pavin (France): Constraints from $\delta^{18}O$ of water and $\delta^{13}C$ of dissolved inorganic carbon: Applied Geochemistry, v. 23, no. 10, p. 2800-2816.

Berg, J. S., Jézéquel, D., Duverger, A., Lamy, D., Laberty-Robert, C., & Miot, J. (2019). Microbial diversity involved in iron and cryptic sulfur cycling in the ferruginous, low-sulfate waters of Lake Pavin. PLOS ONE, 14(2), e0212787.

Calvert, S.E., and Pedersen, T.F., 1996. Sedimentary geochemistry of manganese: Implication for the environment of formation of manganiferous black shales. Economic Geology v. 91, p. 36-47.

Clement, B.G., Luther, G.W. III, Tebo, B.M., 2009. Rapid, oxygen-dependent microbial Mn(II) oxidation kinetics at sub-micromolar oxygen concentrations in the Black Sea suboxic zone. Geochimica et Cosmochimica Acta, v. 73, p. 1878-1889.

Crowe, S., Katsev, S., Leslie, K., Sturm, A., Magen, C., Nomosatryo, S., Pack, M., Kessler, J., Reeburgh, W., and Roberts, J., 2011, The methane cycle in ferruginous Lake Matano: Geobiology, v. 9, no. 1, p. 61-78.

Daye, M., Klepac-Ceraj, V., Pajusalu, M., Rowland, S., Farrell-Sherman, A., Beukes, N., Tamura, N., Fournier, G., and Bosak, T., 2019. Light-driven anaerobic microbial oxidation of manganese. Nature, doi: 10.1038/s41586-019-1804-0.

Ettwig, K.F., Zhu, B., Speth, D., Keltjens, J.T., Jetten, M.S.M., and Kartal, B., 2016. Archaea catalyze iron-dependent anaerobic oxidation of methane. Proceedings of the National Academy of Sciences, v. 113, p, 12792-12796.

Farquhar, J., Zerkle, A.L., and Bekker, A., 2014. 6.4 - Geologic and geochemical constraints on Earth's early atmosphere. Treatise on Geochemistry, v. 6, p. 91-138.

Force, E.R., and Cannon, W.F., 1988. Depositional model for shallow-marine manganese deposits around black shale basins. Economic Geology, v. 83, p. 93-117.

Gumsley, A.P., Chamberlain, K.R., Bleeker, W., Soderlund, U., de Kock, M., Larsson, E.R., and Bekker, A., 2017. Timing and tempo of the Great Oxidation Event. Proceedings of the National Academy of Sciences, v. 114, p. 1811-1816.

Hausler, K., Dellwig, O., Schnetger, B., Feldens, P., Leipe, T., Moros, M., Pollehne, F., Schonke, M., Wegwerth, A., and Arz, H.W., 2018. Massive Mn carbonate formation in the Landsort Deep (Baltic Sea): hydrographic conditions, temporal succession, and Mn budget calculations. Marine Geology v. 395, p. 260-270.

Havig, J.R., Hamilton, T.L., McCormick, M., McClure, B., Sowers, T., Wegter, B., and Kump, L.R., 2017. Water column and sediment stable carbon isotope biogeochemistry of permanently redox-stratified Fayetteville Green Lake, New York, USA. Limnology and Oceanography, v. 63, p, 570-587.

Herndon, E.M., Havig, J.R., Singer, D.M., McCormick, M.L., and Kump, L.R., 2018. Manganese and iron geochemistry in sediments underlying the redox-stratified Fayetteville Green Lake. Geochimica et Cosmochimica Acta, v. 231, p. 50-63.

Jenkyns, H.C., 2010. Geochemistry of ocean anoxic events. Geochemistry, Geophysics, Geosystems, v. 11, doi:10.1029/2009GC002788.

Jiang, C.Z., and Tosca, N.J., 2019. Fe(II)-carbonate precipitation kinetics and the chemistry of anoxic ferruginous seawater. Earth and Planetary Science Letters, v. 506, p. 231-242.

Johnson, J.E., Webb, S.M., Thomas, K., Ono, S., Kirschvink, J.L., and Fischer, W.W., 2013. Manganese-oxidizing photosynthesis before the rise of cyanobacteria. Proceedings of the National Academy of Sciences, v. 110, p. 11238-11243.

Johnson, J.E., Webb, S.M., Ma, C., and Fischer, W.W., 2016. Manganese mineralogy and diagenesis in the sedimentary rock record. Geochimica et Cosmochimica Acta, v. 173, p. 210-231.

Jones, C., Crowe, S.A., Sturm, A., Leslie, K.L., MacLean, L.C.W., Katsev, S., Henry, C., Fowle, D.A., and Canfield, D.E., 2011. Biogeochemistry of manganese in ferruginous Lake Matano, Indonesia: Biogeosciences v. 8., p. 2977-2991

Kirschvink, J.L., Gaidos, E.J., Bertani, E.L., Beukes, N.J., Gutzmer, J., Maepa, L.N., and Steinberger, R.L., 2000. Paleoproterozoic snowball Earth: Extreme climatic and geochemical global change and its biological consequences. Proceedings of the National Academy of Sciences, v. 97, p. 1400-1405.

Lambrecht, N., Wittkop, C., Katsev, S., Fakhraee, M., and Swanner, E.D. Geochemical characterization of two ferruginous meromictic lakes in the Upper Midwest, USA, 2018. Journal of Geophysical Research – Biogeosciences, doi:10.1029/2018JG004587.

Lambrecht, N., Katsev, S., Wittkop, C., Hall, S.J., Sheik, C.S., Picard, A., Fakhraee, M., and Swanner, E.D., 2020. Biogeochemical and physical controls on methane fluxes from two ferruginous meromictic lakes. Geobiology, v. 18, p. 54-69, doi: 10.1111/gbi.12365.

Lantink, M.L., Oonk, P.B.H., Floor, G.H., Tsikos, H., and Mason, P.R.D., 2018. Fe isotopes of a 2.4 Ga hematite-rich IF constrain marine redox conditions around the GOE. Precambrian Research, v. 305, p. 218-235.

Lliros, M., Garcia-Armisen, T., Darchambeau, F., Morana, C., Triado-Margarit, X., Inceoglu, O., Borrego, C.M., Bouillon, S., Servais, P., Borges, A.V., Descy, J-P., Canfield, D.E., and Crowe, S.A., 2015. Pelagic photoferrotrophy and iron cycling in a modern ferruginous basin. Scientific Reports, doi: 10.1038/srep13803.

Lyons, T.W., Reinhard, C.T., and Planavsky, N.J., 2014. The rise of oxygen in Earth's early ocean and atmosphere: Nature, v. 506, p. 307-315.

Maynard, J.B., 2010. The chemistry of manganese ores through time: A signal of increasing diversity of Earth-surface environments. Economic Geology, v. 105, p. 535-552.

Michaelis, W., Seifert, R., Nauhaus, K., Treude, T., Thiel, V., Blumenberg, M., Knittel, K., Gieseke, A., Peterknecht, K., Pape, T., Boetius, A., Amann, R., Jorgensen, B.B., Widdel, F., Peckman, J., Pimenov, N.V., and Gulin, M.B., 2002. Microbial reefs in the Black Sea fueled by anaerobic oxidation of methane. Science, v. 297, p. 1013-1015.

Morse, J.W., Arvidson, R.S., and Luttge, A., 2007. Calcium carbonate formation and dissolution. Chemical Reviews, v. 107, p, 342-381.

Mucci, A., 2004. The behavior of mixed Ca-Mn carbonates in water and seawater: Controls of manganese concentrations in marine porewaters. Aquatic Geochemistry, v. 10, p 139-169.

Myrbo, A., and Shapley, M., 2006, Seasonal water-column dynamics of dissolved inorganic carbon stable isotopic compositions ($\delta^{13}C_{DIC}$) in small hardwater lakes in Minnesota and Montana: Geochimica et Cosmochimica Acta, v. 70, no. 11, p. 2699-2714.

Neubert, N., Nagler, T.F., and Bottcher, M.E., 2008. Sulfidity controls molybdenum isotope fractionation into euxinic sediments: evidence from the modern Black Sea. Geology v. 36, p. 775-778.

Nuhfer, E.B., Anderson, R.Y., Bradbury, J.P., and Dean, W.E., 1993, Modern sedimentation in Elk Lake, Clearwater County, Minnesota, in Bradbury, J.P., and Dean, W.E., eds., Elk Lake, Minnesota: Evidence for rapid climate change in the North-Central United States: Boulder, Colorado, Geological Society of America Special Paper 276, p. 75-96.

Okita, P.M., 1992. Manganese carbonate mineralization in the Molgano District, Mexico. Economic Geology, v. 87, p. 1345-1366.

Ossa Ossa, F., Hofmann, A., Wille, M., Spangenberg, J.E., Bekker, A., Poulton, S.W., Eickmann, B., and Schoenberg, R., 2018a. Aerobic iron and manganese cycling in a redox-stratified Mesoarchean epicontinental sea. Earth and Planetary Science Letters, v. 500, p. 28-40.

Ossa Ossa, F., Eickmann, B., Hofmann, A., Planavsky, N.J., Asael, D., Pambo, F., and Bekker, A., 2018b. Two-step deoxygenation at the end of the Paleoproterozoic Lomagundi Event. Earth and Planetary Science Letters, v. 486, p. 70-83.

Oswald, K., Jegge, C., Tischer, J., Berg, J., Brand, A., Miracle, M.R., Soria, X., Vicente, E., Lehmann, M.F., Zopfi, J., and Schubert, C.J., 2016. Methanotrophy under versatile conditions in the water column of the ferruginous meromictic Lake La Cruz (Spain). Frontiers in Microbiology, v. 7, doi:10.3389/fmicb.2016.01762.

Pingitore, N.E., Eastman, M.P., Sandidge, M., Oden, K., and Freiha, B., 1988. The coprecipitation of Manganese(II) with calcite: an experimental study. Marine Chemistry, v. 25, p. 107-120.

Planavsky, N.J., Asael, D., Hofmann, A., Reinhard, C.T., Lalonde, S.V., Knudsen, A., Wang, X., Ossa Ossa, F., Pecoits, E., Smith, A.J.B., Beukes, N.J., Bekker, A., Johnson, T.M., Konhauser, K.O., Lyons, T.W., and Rouxel, O.J., 2014. Evidence for oxygenic photosynthesis half a billion years before the Great Oxidation Event. Nature Geoscience, v. 7, p. 283-286.

Planavsky, N.J., Slack, J.F., Cannon, W.F., O'Connell, B., Isson, T.T., Asael, D., Jackson, J.C., Hardisty, D.S., Lyons, T.W., and Bekker, A., 2018. Evidence for episodic oxygenication in a weakly redox buffered deep mid-Proterozoic ocean. Chemical Geology, v. 483, p. 581-594.

Poulton, S.W., Fralick, P.W., and Canfield, D.E., 2010. Spatial variability in oceanic redox structure 1.8 billion years ago. Nature Geoscience, v. 3, p. 486-490.

Rincon-Tomas, B., Khonsari, B., Muhlen, D., Wickbold, C., Schafer, N., Hause-Reitner, D., Hoppert, M., and Reitner, J., 2016. Manganese carbonates as possible biogenic relics in Archean settings. International Journal of Astrobiology, v. 15, p. 219-229.

Roy, S., 2006. Sedimentary manganese metallogenesis in response to the evolution of the Earth system. Earth-Science Reviews, v. 77, p. 273-305.

Song, H., Jiang, G., Poulton, S.W., Wignall, P.B., Tong, J., Song, H., An, Z., Chu, D., Tian, L., She, Z., and Wang, C., 2017. The onset of widespread marine red beds and the evolution of ferruginous oceans. Nature Communications, doi: 10.1038/s41467-017-00502-x

Stevens, L.R., Ito, E., and Olson, D.E.L., 2000. Relationship of Mn-carbonates in varved lake-sediments to catchment vegetation in Big Watab Lake, MN, USA. Journal of Paleolimnology, v. 24, p. 199-211.

Sturm, A., Fowle, D.A., Jones, C., Leslie, K., Nomosatryo, S., Henry, C., Canfield, D.E., and Crowe, S.A., 2019. Rates and pathways of CH4 oxidation in ferruginous Lake Matano, Indonesia. Geobiology, v. 17, p. 294-307.

Thamdrump, B., Fossing, H., and Jorgensen, B.B., 1994. Manganese, iron, and sulfur cycling in a coastal marine sediment, Aarhus Bay, Denmark. Geochimica et Cosmochimica Acta, v. 58, p. 5115-5129.

Tsikos, H., Matthews, A., Erel, Y., and Moore, J.M., 2010. Iron isotopes constrain biogeochemical redox cycling of iron and manganese in a Paleoproterozoic stratified basin. Earth and Planetary Science Letters, v. 298, p. 125-134.

Van Cappellen, P., Viollier, E., Roychoudhury, A., Clark, L., Ingall, E., Lowe, K., and Dichristina, T., 1998. Manganese and Iron at the oxic-anoxic transition of a stratified marine basin (Orca Basin, Gulf of Mexico). Environmental Science and Technology, v. 32, p. 2931-2939.

Walter, X.A., Picazo, A., Miracle, M.R., Vicente, E., Camacho, A., Aragno, M., and Zopfi, J., 2014. Phototrophic Fe(II)-oxidation in the chemocline of a ferruginous meromictic lake. Frontiers in Microbiology, doi: 10.3389/fmicb.2014.00713.

Winter, B. L., and Knauth, L. P., 1992, Stable isotope geochemistry of cherts and carbonates from the 2.0 Ga Gunflint Iron Formation: implications for the depositional setting, and the effects of diagenesis and metamorphism: Precambrian Research, v. 59, no. 3, p. 283-313.

Wittkop, C., Teranes, J., Lubenow, B., and Dean, W.E., 2014, C- and O-stable isotopic signatures of methanogenesis, temperature, and water column stratification in Holocene siderite varves. Chemical Geology, v. 389, p. 153-166.

Figure 1

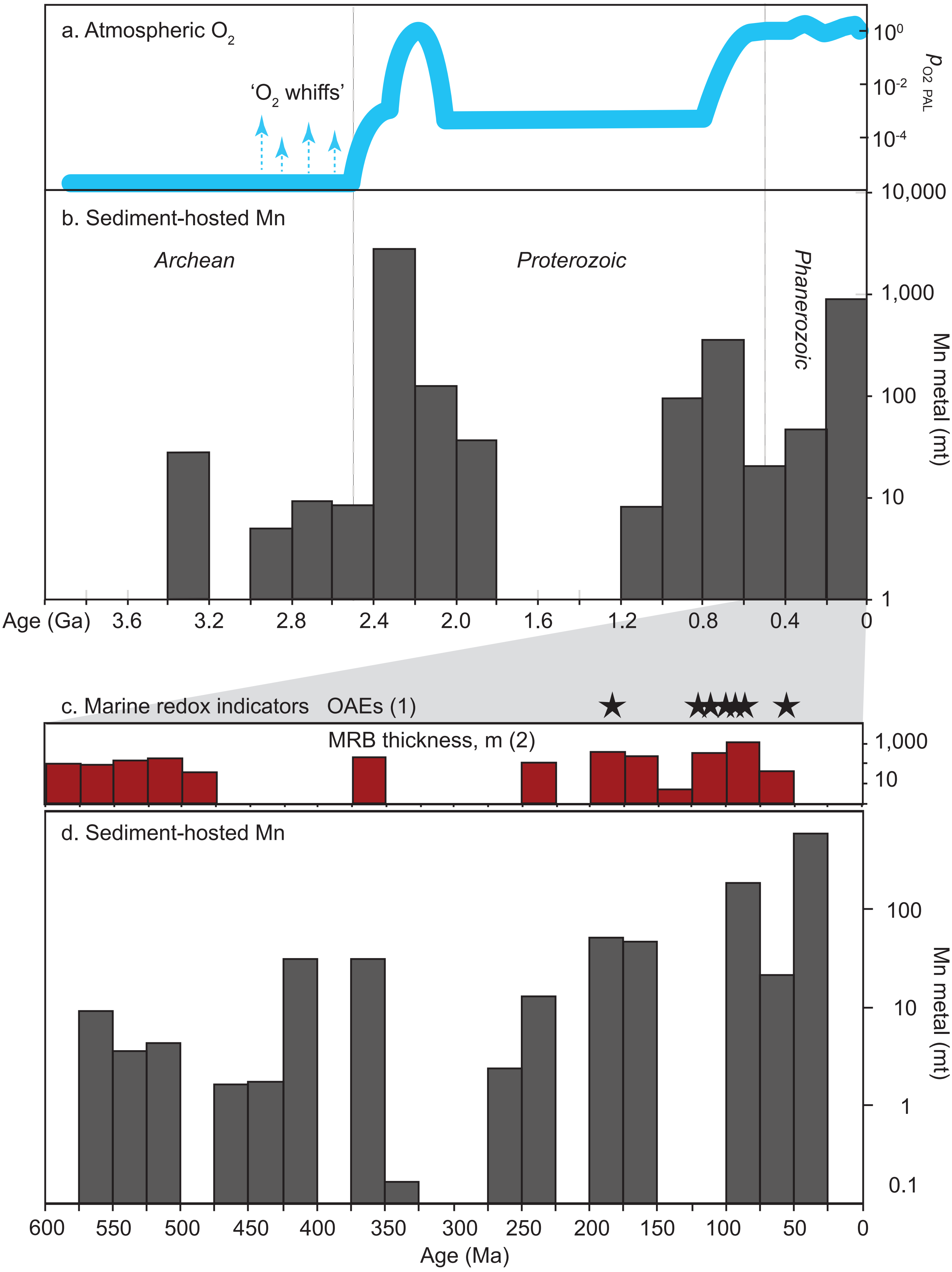
a. Atmospheric O_2
'O_2 whiffs'
10^0
10^{-2}
10^{-4}
$p_{O_2\ PAL}$
b. Sediment-hosted Mn
Archean
Proterozoic
Phanerozoic
10,000
1,000
100
10
1
Mn metal (mt)
Age (Ga)
3.6
3.2
2.8
2.4
2.0
1.6
1.2
0.8
0.4
0
c. Marine redox indicators
OAEs (1)
MRB thickness, m (2)
1,000
10
d. Sediment-hosted Mn
100
10
1
0.1
Mn metal (mt)
600
550
500
450
400
350
300
250
200
150
100
50
0
Age (Ma)

Figure 2

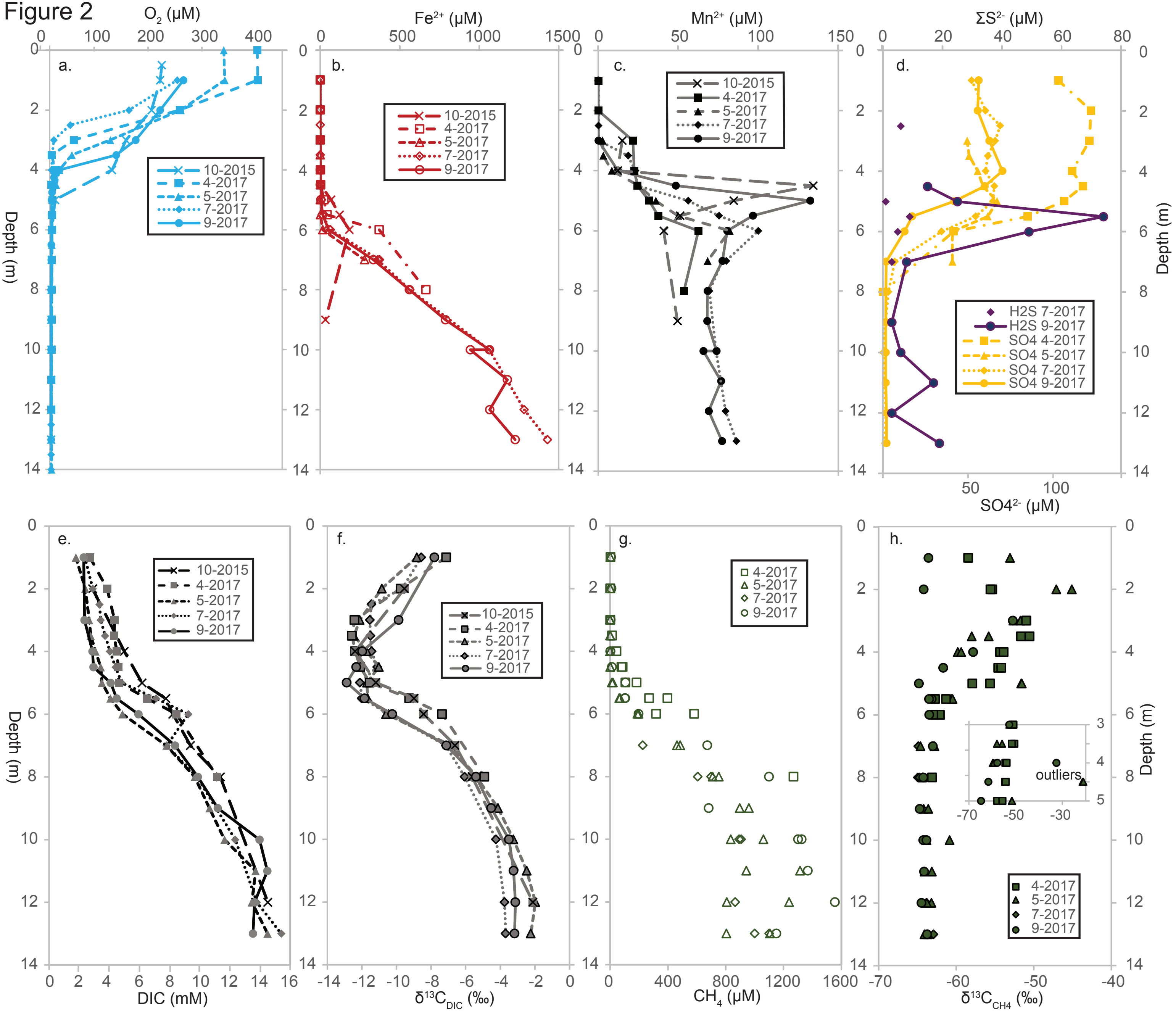
O$_2$ (µM)
0 100 200 300 400
a.
10-2015
4-2017
5-2017
7-2017
9-2017
Depth (m)
0 2 4 6 8 10 12 14
Fe^{2+} (µM)
0 500 1000 1500
b.
10-2015
4-2017
5-2017
7-2017
9-2017
Mn^{2+} (µM)
0 50 100 150
c.
10-2015
4-2017
5-2017
7-2017
9-2017
ΣS^{2-} (µM)
0 20 40 60 80
d.
H2S 7-2017
H2S 9-2017
SO4 4-2017
SO4 5-2017
SO4 7-2017
SO4 9-2017
50 100
SO4^{2-} (µM)
Depth (m)
e.
10-2015
4-2017
5-2017
7-2017
9-2017
0 2 4 6 8 10 12 14 16
DIC (mM)
f.
10-2015
4-2017
5-2017
7-2017
9-2017
-14 -12 -10 -8 -6 -4 -2 0
δ^{13}C$_{DIC}$ (‰)
g.
4-2017
5-2017
7-2017
9-2017
0 400 800 1200 1600
CH$_4$ (µM)
h.
3 4 5
outliers
-70 -50 -30
4-2017
5-2017
7-2017
9-2017
-70 -60 -50 -40
δ^{13}C$_{CH4}$ (‰)
Depth (m)

Figure 3

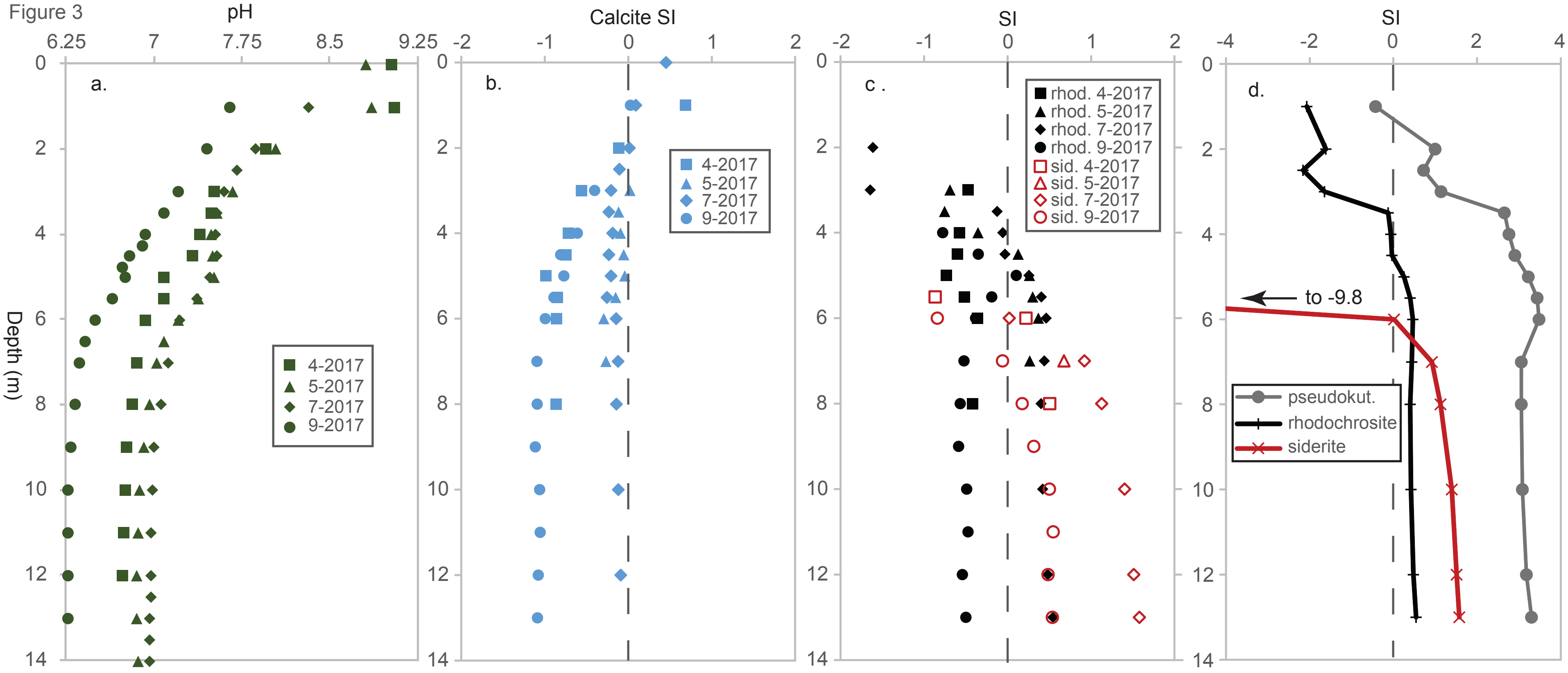
pH
6.25
7
7.75
8.5
9.25
a.
4-2017
5-2017
7-2017
9-2017
Depth (m)
0
2
4
6
8
10
12
14
Calcite SI
-2
-1
0
1
2
b.
4-2017
5-2017
7-2017
9-2017
SI
c .
rhod. 4-2017
rhod. 5-2017
rhod. 7-2017
rhod. 9-2017
sid. 4-2017
sid. 5-2017
sid. 7-2017
sid. 9-2017
SI
-4
-2
0
2
4
d.
to -9.8
pseudokut.
rhodochrosite
siderite

Figure 4

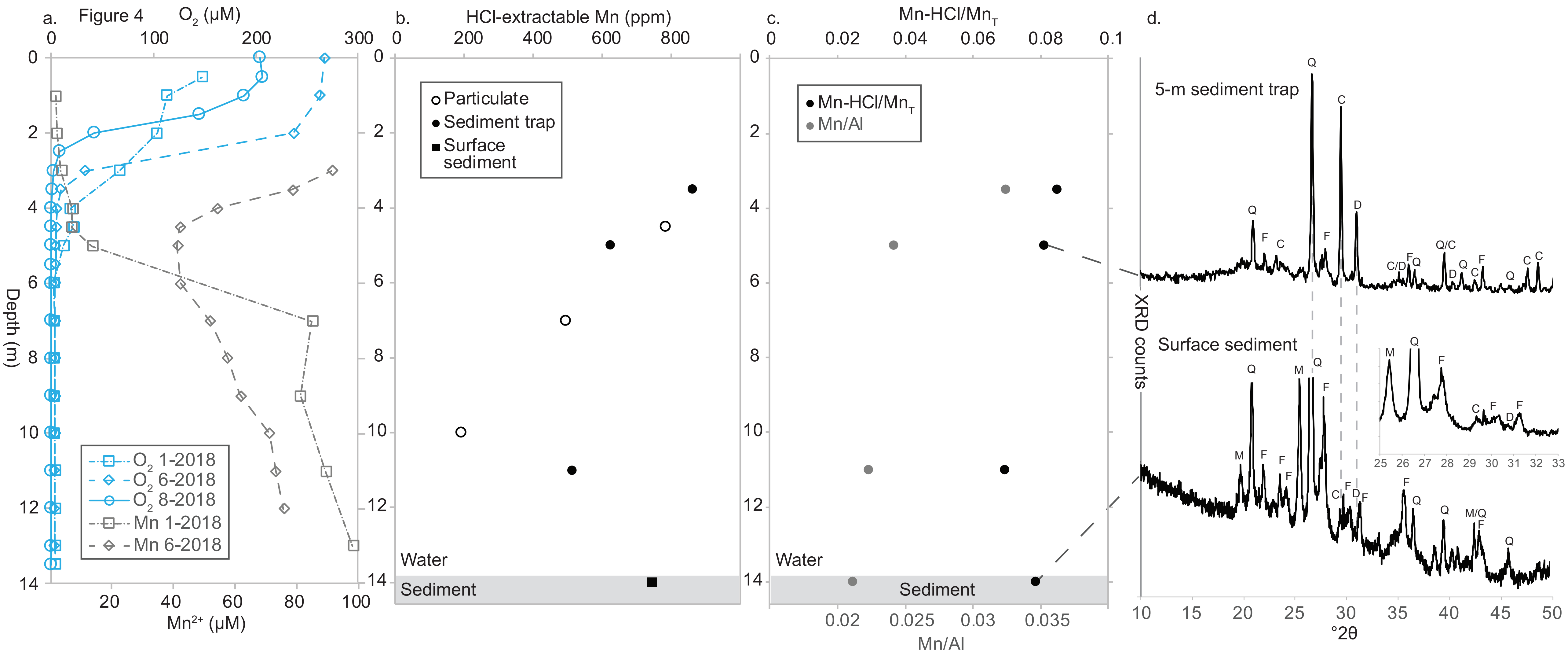
a.
O$_2$ (µM)
0
100
200
300
Depth (m)
Mn^{2+} (µM)
20
40
60
80
100
O$_2$ 1-2018
O$_2$ 6-2018
O$_2$ 8-2018
Mn 1-2018
Mn 6-2018
b.
HCl-extractable Mn (ppm)
200
400
600
800
○ Particulate
● Sediment trap
■ Surface sediment
Water
Sediment
c.
Mn-HCl/Mn$_T$
0.02
0.04
0.06
0.08
0.1
● Mn-HCl/Mn$_T$
● Mn/Al
Water
Sediment
Mn/Al
0.02
0.025
0.03
0.035
0
2
4
6
8
10
12
14
d.
5-m sediment trap
Surface sediment
XRD counts
°2θ
10
15
20
25
30
35
40
45
50
Q
F
C
D
C/D
Q/C
M
M/Q
25
26
27
28
29
30
31
32
33

Figure 5

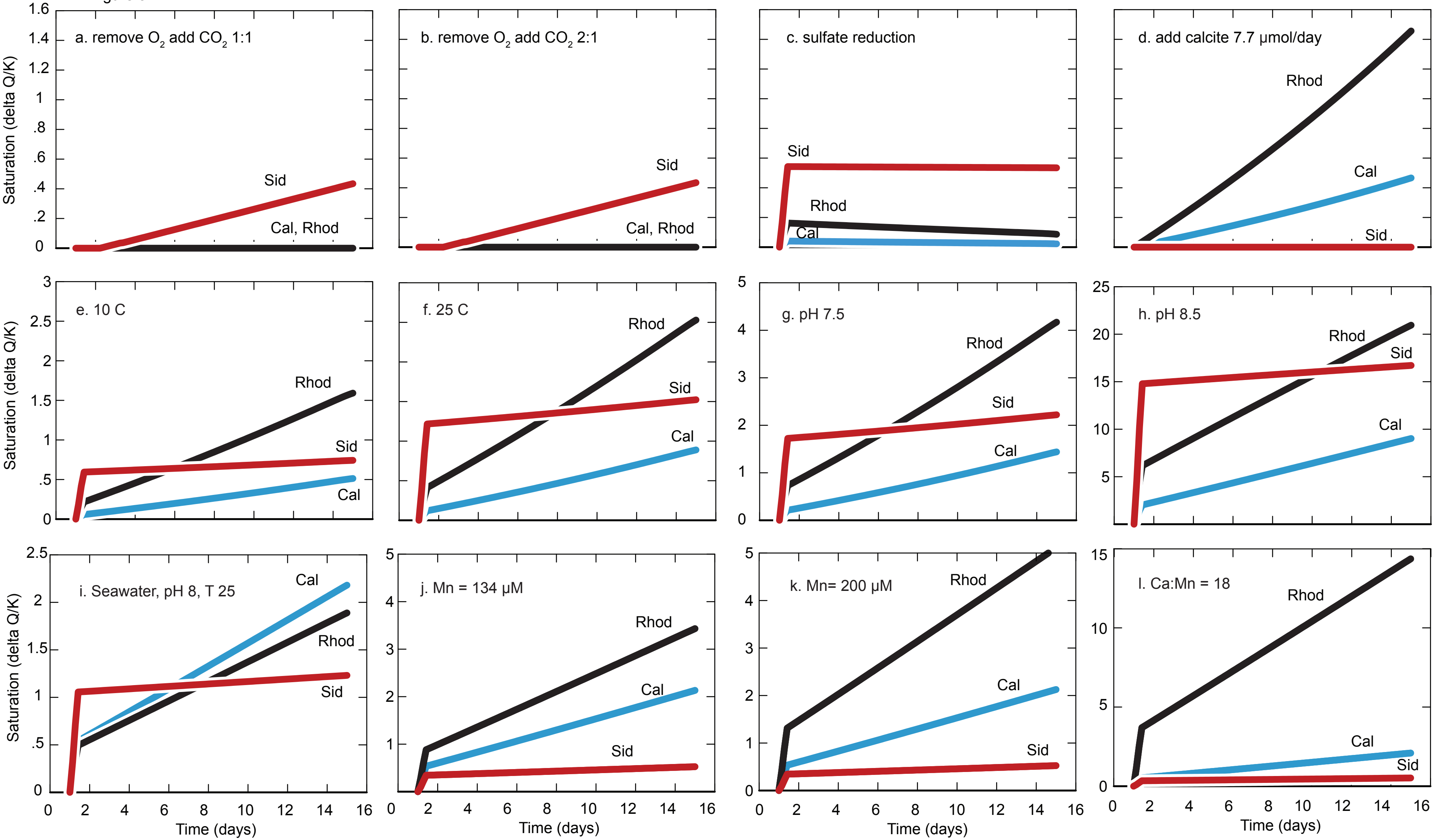

a. remove O_2 add CO_2 1:1

b. remove O_2 add CO_2 2:1

c. sulfate reduction

d. add calcite 7.7 μmol/day

e. 10 C

f. 25 C

g. pH 7.5

h. pH 8.5

i. Seawater, pH 8, T 25

j. Mn = 134 μM

k. Mn= 200 μM

l. Ca:Mn = 18

Figure 6

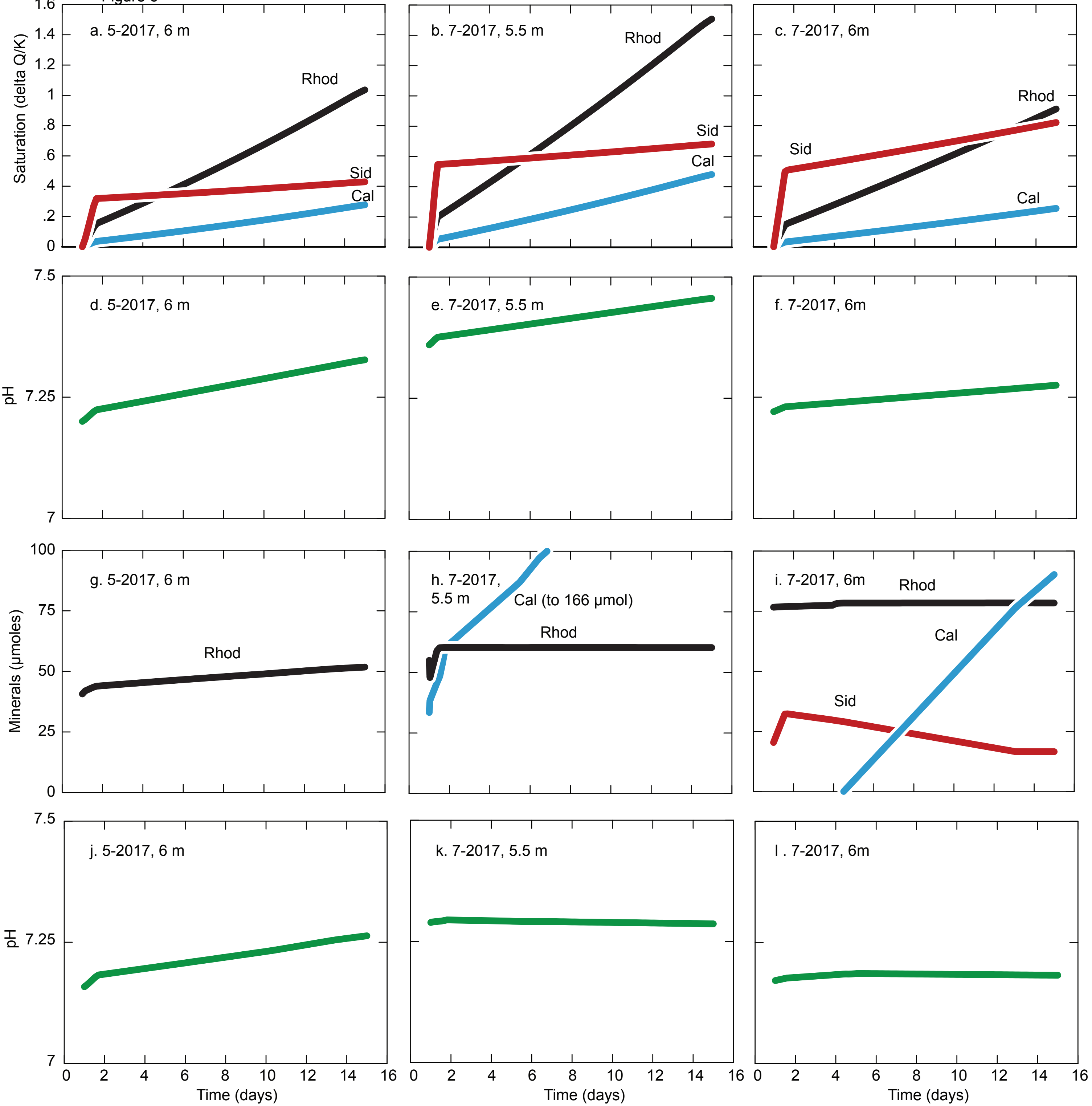

Saturation (delta Q/K)
1.6
1.4
1.2
1
.8
.6
.4
.2
0
a. 5-2017, 6 m
Rhod
Sid
Cal
b. 7-2017, 5.5 m
Rhod
Sid
Cal
c. 7-2017, 6m
Rhod
Sid
Cal
pH
7.5
7.25
7
d. 5-2017, 6 m
e. 7-2017, 5.5 m
f. 7-2017, 6m
Minerals (µmoles)
100
75
50
25
0
g. 5-2017, 6 m
Rhod
h. 7-2017, 5.5 m
Cal (to 166 µmol)
Rhod
i. 7-2017, 6m
Rhod
Cal
Sid
pH
7.5
7.25
7
j. 5-2017, 6 m
k. 7-2017, 5.5 m
l . 7-2017, 6m
0
2
4
6
8
10
12
14
16
Time (days)
Time (days)
Time (days)

Figure 7

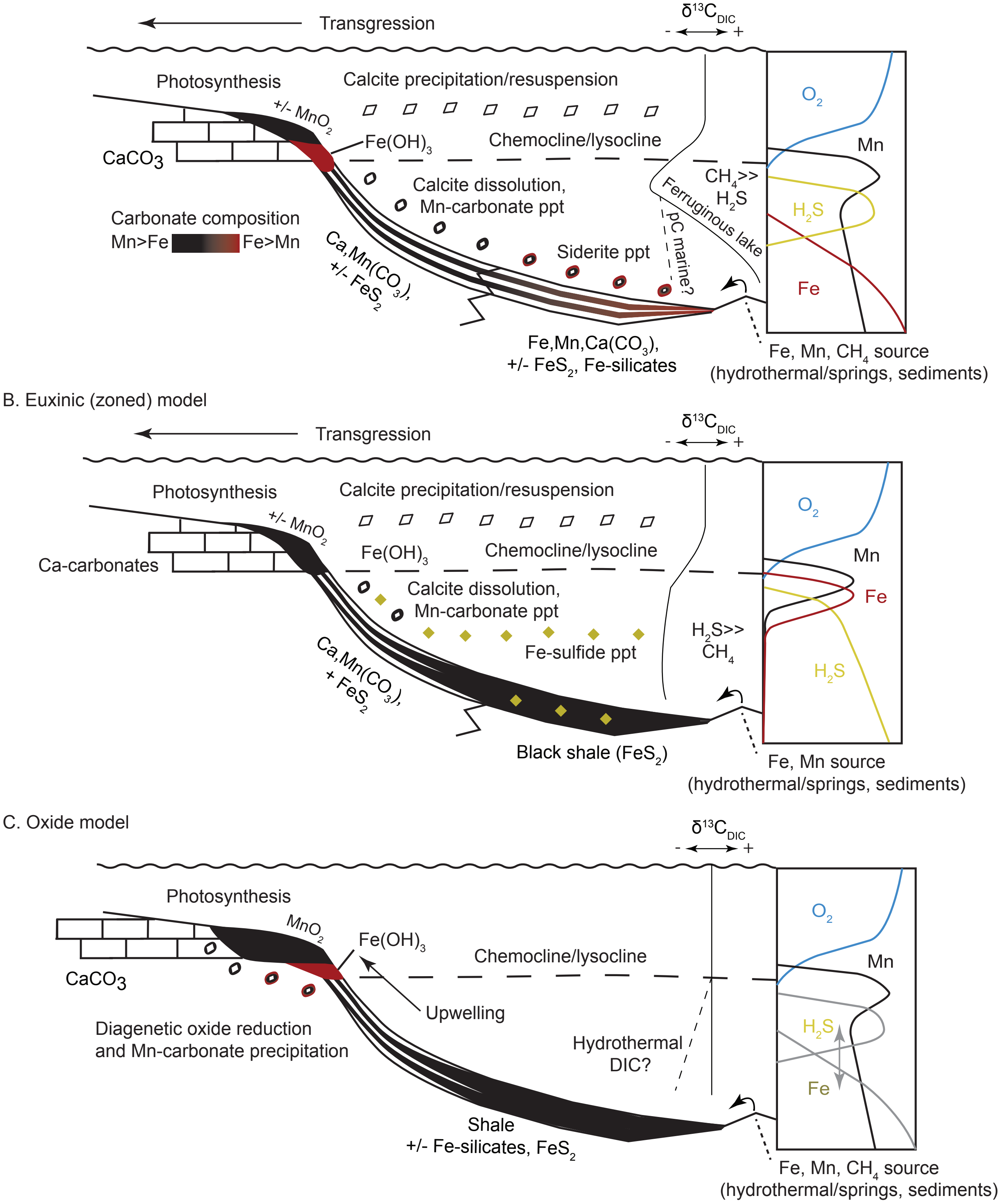
A. Carbonate model (this study)
Transgression
$\delta^{13}C_{DIC}$
- +
Photosynthesis
Calcite precipitation/resuspension
+/- MnO_2
$Fe(OH)_3$
Chemocline/lysocline
$CaCO_3$
O_2
Mn
CH_4>> H_2S
H_2S
Fe
Calcite dissolution, Mn-carbonate ppt
Carbonate composition
Mn>Fe Fe>Mn
Ca,Mn(CO_3), +/- FeS_2
Siderite ppt
Ferruginous lake
pC marine?
Fe,Mn,Ca(CO_3), +/- FeS_2, Fe-silicates
Fe, Mn, CH_4 source (hydrothermal/springs, sediments)
B. Euxinic (zoned) model
Transgression
$\delta^{13}C_{DIC}$
- +
Photosynthesis
Calcite precipitation/resuspension
+/- MnO_2
Ca-carbonates
$Fe(OH)_3$
Chemocline/lysocline
O_2
Mn
Fe
Calcite dissolution, Mn-carbonate ppt
H_2S>> CH_4
Fe-sulfide ppt
H_2S
Ca,Mn(CO_3), + FeS_2
Black shale (FeS_2)
Fe, Mn source (hydrothermal/springs, sediments)
C. Oxide model
$\delta^{13}C_{DIC}$
- +
Photosynthesis
MnO_2
$Fe(OH)_3$
$CaCO_3$
Chemocline/lysocline
O_2
Mn
H_2S
Fe
Upwelling
Diagenetic oxide reduction and Mn-carbonate precipitation
Hydrothermal DIC?
Shale +/- Fe-silicates, FeS_2
Fe, Mn, CH_4 source (hydrothermal/springs, sediments)

Wittkop et al., in press. Table 1.

Interval	May 2017 6m		July 2017 5.5m		July 2017 6m		Seawater / July 2017 5.5m	
Species	Conc.	Units	Conc.	Units	Conc.	Units	Conc.	Units
Al^{3+}	-	-	0.371	μmol/L	0.408	μmol/L	0.371	μmol/L
$B(OH_4)^-$	2.868	μmol/L	6.753	μmol/L	6.660	μmol/L	6.753	μmol/L
Ca^{2+}	1906	μmol/L	1933	μmol/L	2008	μmol/L	10.28	mmol/kg
Cr^{3+}	0.019	μmol/L	0.019	μmol/L	0.038	μmol/L	0.019	μmol/L
Fe^{2+}	15.40	μmol/L	11.76	μmol/L	63.57	μmol/L	11.76	μmol/L
K^+	206.20	μmol/L	192.16	μmol/L	220.52	μmol/L	10.2	mmol/kg
Mg^{2+}	720.6	μmol/L	749.3	μmol/L	795.8	μmol/L	52.8	mmol/kg
Mn^{2+}	82.15	μmol/L	75.45	μmol/L	99.99	μmol/L	571	μmolar
Na^+	15046	μmol/L	14720	μmol/L	16666	μmol/L	469	mmol/kg
Cl^-	20164	μmol/L	16931	μmol/L	18482	μmol/L	546	mmol/kg
Br^-	33.79	μmol/L	3.755	μmol/L	5.006	μmol/L	0.84	mmol/kg
SO_4^{2-}	40.60	μmol/L	54.13	μmol/L	34.35	μmol/L	54.13	μmol/L
HPO_4^{2-}	0.293	μmol/L	0.592	μmol/L	0.907	μmol/L	0.592	μmol/L
O_2	4.1	μmol/L	3.13	μmol/L	2.8	μmol/L	3.1	μmol/L
H^+	7.2	pH	7.36	pH	7.22	pH	8	pH
HCO_3^-	4.4	mM	6.5	mM	8.4	mM	1.77	mmol/kg
NO_3^-	-	-	-	-	0.1290	μmol/L	-	-
T	7.58	°C	8.33	°C	7.58	°C	25	°C
Ca/Mn	23		26		20		18	
Mn/Fe	5.3		6.4		1.6		49	
Reactant	Rate (μM/day)		Rate (μM/day)		Rate (μM/day)		Rate (μM/day)	
O_2	-0.27		-0.21		-0.19		-0.21	
CO_2	0.14		0.10		0.09		0.10	
Calcite	7.70		7.70		7.70		7.70	
SO^{42-}	-2.71		-3.61		-2.29		-3.61	
H_2S	2.71		3.61		2.29		3.61	
HCO_3^-	5.41		7.22		4.58		7.22	